

Classical Chaos in Quantum Computers

Simon-Dominik Börner,¹ Christoph Berke,¹ David P. DiVincenzo,^{2,3,4} Simon Trebst,¹ and Alexander Altland¹

¹*Institute for Theoretical Physics, University of Cologne, 50937 Cologne, Germany*

²*Institute for Quantum Information, RWTH Aachen University, 52056 Aachen, Germany*

³*Jülich-Aachen Research Alliance (JARA), Fundamentals of Future Information Technologies, 52425 Jülich, Germany*

⁴*Peter Grünberg Institute, Theoretical Nanoelectronics, Forschungszentrum Jülich, 52425 Jülich, Germany*

The development of quantum computing hardware is facing the challenge that current-day quantum processors, comprising 50-100 qubits, already operate outside the range of quantum simulation on classical computers. In this paper we demonstrate that the simulation of *classical* limits can be a potent diagnostic tool potentially mitigating this problem. As a testbed for our approach we consider the transmon qubit processor, a computing platform in which the coupling of large numbers of nonlinear quantum oscillators may trigger destabilizing chaotic resonances. We find that classical and quantum simulations lead to similar stability metrics (classical Lyapunov exponents vs. quantum wave function participation ratios) in systems with $\mathcal{O}(10)$ transmons. However, the big advantage of classical simulation is that it can be pushed to large systems comprising up to thousands of qubits. We exhibit the utility of this classical toolbox by simulating all current IBM transmon chips, including the recently announced 433-qubit processor of the Osprey generation, as well as future devices with 1,121 qubits (Condor generation). For realistic system parameters, we find a systematic increase of Lyapunov exponents with system size, suggesting that larger layouts require added efforts in information protection.

I. INTRODUCTION

Coupled mathematical pendula are textbook paradigms of deterministic classical chaos [1]. When excited to energies large enough that the nonlinearity of the pendulum potential becomes sizeable, a transition from integrable harmonic motion to chaotic dynamics generically takes place. In the world of quantum physics, the mathematical pendulum finds a prominent realization as the transmon superconducting qubit [2], with the ‘gravitational potential’ defined by a Josephson junction, and the ‘kinetic energy’ by a micro capacitor. The cosine nonlinearity of the former is required to gap the lowest two quantum states of the transmon (aka the qubit) against the noncomputational higher lying parts of the spectrum in a non-resonant manner [3, 4]. Coupled transmons/pendula define the brickwork of superconducting quantum processors [5]. On the basis of quantum-to-classical correspondence, one may suspect traces of chaotic dynamics – which are toxic where quantum computing is concerned – to be visible in this setting [6, 7]. Indeed, they are, and there appear to be two master strategies for keeping them out: decouple qubits off-operation by so-called tunable couplers [8–10] (an approach applied in, e.g., Google’s Sycamore quantum chip [11]), or intentionally detune the oscillator frequencies of neighboring qubits relative to each other, to avoid dangerous resonances (as done in current quantum chips by the IBM [12] / Delft [13] / ETH Zürich [14] consortia).

Both approaches have their individual advantages. The first reliably stabilizes the system, but at the expense of substantial overhead hardware for switchable coupling [11]. The second avoids this complication, but instead introduces engineered *disorder*. (In the parlance of quantum many-body physics, the ensuing state of matter is called ‘many-body localized’ [15, 16]. In it, the system becomes effectively integrable, but at the expense of site to site randomness, with perhaps unintended side effects in large-scale structures.)

In this paper, we investigate manifestations of *classical* chaos in transmon arrays, tuned to a classical limit by set-

ting $\hbar = 0$ [17]. Otherwise, our systems – their transmon frequencies, coupling strength, system layout, etc. – are modeled in agreement with published data for existing quantum chips [18, 19]. Why would one enforce a classical limit upon a quantum computer? Our prime motivation for this study is that the transmon array displays a highly developed quantum-to-classical correspondence: exact diagonalization performed for the corresponding *quantum* systems show quantum chaos in parametric regions with classical chaos, and its absence in regions without. For systems with up to ten transmons (the limit for our quantum calculations), this correspondence is developed with high accuracy. The point now is that the analysis of the classical limit can be pushed to $\mathcal{O}(10^3)$ resonators, i.e., numbers comparable to those of state-of-art processors deployed in cloud computing services [18], and way beyond anything that can be quantum simulated on a classical computer. Our study of *large-scale*, but *static* transmon storage devices complements the existing literature on the link between classical chaos and the driven quantum dynamics in circuit QED set-ups [17, 20, 21]. While these earlier works study the effects of nonlinearities in circuits subject to additional complexity, e.g., with drive lines for the implementation of gates, they focus on *small-scale* architectures (single qubit coupled to a cavity).

Our construction of classical dynamics simulations as a diagnostic toolbox for large scale processor layouts is organized in three steps. After a quick review of current day transmon hardware in Section II, we present an analysis of classical chaos in linear arrays of two to ten transmons in Section III. A principal observation is that chaos is present already in the two-transmon context but only at excitation energies way beyond those relevant for quantum applications. For ten transmons, however, manifestations of chaos bleed down into the excitation range corresponding to that of the quantum computational qubit Hilbert space. We take this observation as an incentive for a thorough comparison of classical and quantum dynamics for ten transmon arrays in Section IV. The number ‘10’ is special inasmuch as it defines the maximal number of

transmons for which we can run precision quantum simulation with good statistics [22].

Focusing on classical Lyapunov exponents and many-body wave function statistics as prime indicators of classical and quantum chaos, respectively, we will construct a comparison chart showing the predictive potential of classical simulation. Specifically, we will argue that Lyapunov exponents measuring the instability of the classical system are, in a statistical sense, in quantitative correspondence to the quantum system's inverse participation ratios (IPR). The latter are a measure for the spread of quantum wave function over Fock space, and provide microscopic information on the integrity of qubits [23].

In Section V we then turn to the trump card of the classical approach, the option to simulate arrays of up to thousands of transmons, including realistic transmon wiring [24] and other hardware design elements. Specifically, we will simulate transmon chips contained in the current IBM roadmap [25], from the 27-transmon Falcon to the announced 1,021-transmon Condor chip. Assuming that the quantum-to-classical correspondence observed at 10-transmon level extends to larger qubit numbers, this analysis yields valuable insights into the design of (future) processor layouts. We will consider advanced design principles, as realized in frequency-engineered cross resonance architectures [26], where IPRs close to unity – representing perfect single transmon wave function localization – can be reached by engineered fine tuning [12, 19]. Our classical analysis will demonstrate the manner in which the Lyapunov exponents signal the proximity to such sweet spots. At the same time, they show a systematic tendency to increase for larger system architectures, which we take as indication that maintaining the stability of these sophisticated designs will require an additional engineering effort. We conclude in section VI.

II. TRANSMON HARDWARE

Transmon-based quantum computers are among the most developed information processing platforms of the NISQ era [27] and have been used in several recent experimental landmarks: the first demonstration of quantum computational advantage [11], the simulation of topologically ordered states [28], and small instances of error-correcting experiments with surface code logical qubits [13, 29]. While there are other promising approaches based on superconducting circuits at the level of single qubits or few-qubit devices (e.g., the fluxonium [30, 31] or the C-shunt flux qubit [32]), transmons are the clear front-runner when it comes to integrating $\mathcal{O}(50)$ – $\mathcal{O}(100)$ qubits into a single viable processor. This property makes the transmon the preferred choice for applications where scalability is paramount, e.g., the recent demonstration of the performance improvement of a logical qubit with the surface code distance, conducted in a 72-qubit device [29]. Processors containing more than 1,000 transmon qubits are expected to be launched in upcoming years. For example, IBM's quantum roadmap announces a monolithic processor with 1,121 qubits for the year 2023 and a modular quantum

computer with 4,158 qubits in 2025 [25].

In the following, we review the transmon qubit array and introduce a model which stays close to the systems used in reality. We then proceed to address the main question of this paper: what can we learn from the *classical* physics of this system about the functioning of the *quantum* processor?

A. Transmons

In its simplest form, a single transmon consists of only a single Josephson junction and a large shunting capacitance. Its Hamiltonian is given by [2]

$$\hat{H}_{\text{Tr}} = 4E_C \hat{n}^2 - E_J \cos \hat{\varphi}, \quad (1)$$

where \hat{n} is the charge operator [33] counting the number of Cooper pairs that have traversed the junction and $\hat{\varphi}$ is the superconducting phase conjugate to \hat{n} , i.e., $[\hat{\varphi}, \hat{n}] = i$. The Josephson energy E_J is a macroscopic parameter describing the ability of Cooper pairs to pass the tunnel barrier, and E_C is the charging energy necessary to transfer one electron through the junction. E_C is proportional to the total capacitance of the circuit and – due to the sizeable shunting capacitance – can be made small compared to E_J , which pushes the dimensionless parameter E_J/E_C to the transmon regime where $E_J/E_C \gtrsim 20$. Typical values of E_C range from 100 MHz to 400 MHz [4], while E_J often lies near 12.5 GHz (note here that we give energies in Hz, by setting \hbar to 1). The ground state and the first excited state serve as the two qubit states $|0\rangle$ and $|1\rangle$. The energy spacing between the two qubit states $\hbar\nu_{01}$ typically takes values of $\nu_{01} \equiv \nu_q = 5$ GHz, where ν_q is called the qubit frequency.

For our purposes, it will be advantageous to consider $\hat{\varphi}$ as an angular variable with conjugate angular momentum $\hat{L}_z = \hbar \hat{n}$. With the identification $E_C = \hbar^2/8ml^2$, and $g = E_J/ml = 8E_C E_J l/\hbar^2$, Eq. (1) then describes a quantum pendulum (see Fig. 1)

$$\hat{H}_{\text{Tr}} = \frac{\hat{L}_z^2}{2ml^2} - mgl \cos \hat{\varphi} \quad (2)$$

of mass m , rigid length l , and gravitational constant g .

The *coupling* of neighboring transmons is often realized via a capacitive interaction $\hat{n}_i \hat{n}_j$ between their charge degrees of freedom. The full Hamiltonian of an array of coupled transmons then reads [34]

$$\hat{H} = 4E_C \sum_i \hat{n}_i^2 - \sum_i E_{J,i} \cos \hat{\varphi}_i + T \sum_{\langle i,j \rangle} \hat{n}_i \hat{n}_j. \quad (3)$$

Here, the site dependence of the Josephson energies, $E_{J,i}$, accounts for unavoidable fabrication imprecisions, usually of the order of 5% to 10% [35, 36]. While these tolerances can be reduced by post-processing or by advanced fabrication techniques (see Ref. [7] for a detailed discussion) frequency variations are often introduced intentionally to detune neighboring transmons during ‘gate-off’ times and in this way suppress undesired correlations [37]. (Adjustable Josephson energy variations are usually realized via so-called flux tunable

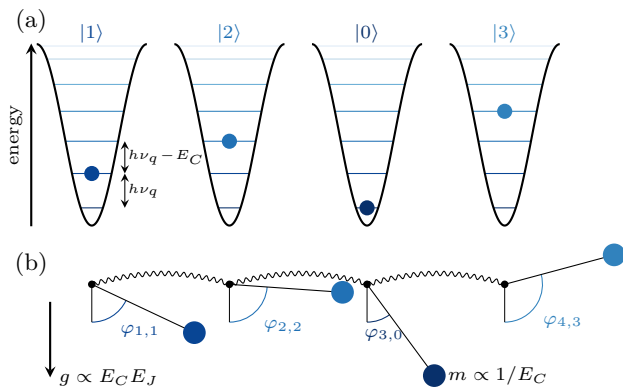


FIG. 1. **Quantum vs. classical transmon array.** (a) A chain of four transmons initialized in the quantum state $|1203\rangle$ of the corresponding cos-potentials, where the integers, $i = 1, 2, 0, 3$ correspond to the bound state energies E_i . (b) The corresponding classical rotors, initialized at angular deflections corresponding to the energies E_i as discussed in the main text, and the springs connecting the suspension points representing the angular momentum coupling.

transmons where a single Josephson interface is replaced by a SQUID [37].)

By comparison, variations of both the charging energy E_C (here assumed to be at the value 250 MHz) and of the coupling energies T (~ 30 MHz for flux tunable transmons[37] and $\sim 3\text{--}5$ MHz [38] for single-junction ‘fixed-frequency’) are of lesser relevance and will be ignored throughout. We also will not consider the important concept of tunable couplers [8], i.e., additional hardware allowing to vary the coupling on operation at the expense of extra noise sources.

B. Classical limit

Transmon quantum computing relies on the deep quantization of the Josephson junctions’ two lowest energy levels. However, as we are going to demonstrate in the following, the system’s classical limit – a network of classical pendula – contains valuable information about the physics of the transmon array. In this limit, the operators $\hat{\varphi}_i, \hat{n}_i$ are demoted to real valued variables φ_i, n_i , and the commutation relation $[\hat{\varphi}_i, \hat{n}_j] = i\delta_{i,j}$ turns into a Poisson bracket

$$\{\varphi_i, n_j\} = \delta_{i,j}. \quad (4)$$

Hamilton’s canonical equations of motion then read

$$\dot{\varphi}_i = \{\varphi_i, H\} = \frac{\partial H}{\partial n_i} = 8E_C n_i + T \sum_{j=\text{NN}(i)} n_j, \quad (5)$$

$$\dot{n}_i = \{n_i, H\} = -\frac{\partial H}{\partial \varphi_i} = -E_{J,i} \sin \varphi_i, \quad (6)$$

where H is the classical Hamilton function obtained by replacing $\hat{\varphi}$ and \hat{n} with their classical counterparts in the Hamiltonian \hat{H} in Eq. (3), and the sum is over nearest neighbors

of transmons. These equations describe a system of classical pendula with a ‘momentum-momentum’ interaction arising from the capacitive coupling.

To mimic a transmon initialized in one of its eigenstates $|0\rangle, |1\rangle, |2\rangle, \dots$ we first compute the energies E_a of the quantum model, where $a = 0, 1$ for computational states. We then initialize the classical rotor in a phase space configuration $(n, \varphi) = (0, \varphi_a)$, where $-E_J \cos \varphi_a = E_a$, or

$$\varphi_a = \arccos\left(-\frac{E_a}{E_J}\right). \quad (7)$$

In other words, the classical pendulum is started in a configuration of maximal potential and zero kinetic energy, see Fig. 1. As illustrated, the quantum transmon supports 7 bound states, for the chosen parameters of $E_J = 12.5$ GHz and $E_C = 250$ MHz, and we distinguish between as many classical initial configurations.

III. CLASSICAL CHAOS

Coupled nonlinear pendula are a paradigm of deterministic chaos, and the question to be addressed in this paper is to what extent the corresponding instabilities also affect the quantum array. To approach this question, we first consider simple toy models: two coupled pendula, and the generalization to a chain of L of them.

A. Two coupled transmons

Chaotic behavior already emerges in the classical two-transmon Hamiltonian, provided that the system is excited to sufficiently high energies [39]. In this reduced setting, the phase space spanned by the coordinates $(n_1, n_2, \varphi_1, \varphi_2)$ is four dimensional, implying that the onset of chaos can be demonstrated via the powerful concept of Poincaré sections, i.e., stroboscopic images defined by the crossing of classical trajectories on the three-dimensional surface of conserved energy with the two-dimensional surface defined by the fixation of one of the coordinates. To be specific, we here keep track of the pairs (φ_1, n_1) at $\varphi_2 = 0$ and $n_2 > 0$, where the second condition fixes a sense of traversal.

To monitor the onset of irregular dynamics, we vary the initial angle φ_2^{init} while keeping $\varphi_1^{\text{init}} = n_2^{\text{init}} = 0$ and $n_1^{\text{init}} = 0.01$ fixed. Fig. 2 shows four different Poincaré sections for initial angles φ_2^{init} , which – from (a) to (d) – get progressively closer to π . While the closed curves for (a) and (b) indicate that the motion is (quasi)periodic and thus integrable, one observes a qualitative change upon further increasing φ_2^{init} . The Poincaré section then extends over a finite fraction of the $\varphi_1\text{--}n_1$ plane, as is expected for nonintegrable systems. We have also confirmed that in the non-integrable regions of the Poincaré plot there is exponential sensitivity to initial conditions, as witnessed by finite Lyapunov exponents. Fig. 3, which is a fine-grained representation of the section (c) in Fig. 2, indeed shows various textbook signatures [40] of a system whose

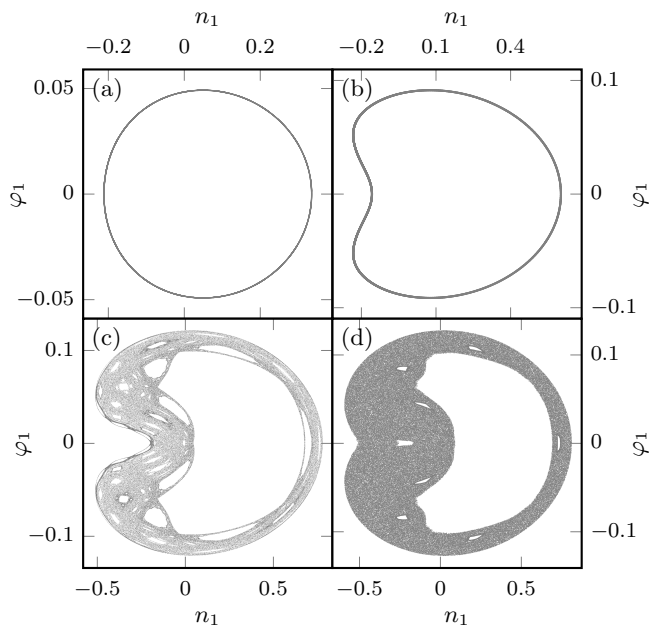


FIG. 2. Poincaré sections for a system of two coupled transmons. Shown are Poincaré sections in the φ_1 - n_1 plane with $\varphi_2 = 0$ and $n_2 > 0$. The transmons are initialized with $\varphi_1(t=0) = n_2(0) = 0$, $n_1(0) = 0.01$ and $\varphi_2 = \pi - x$, where (a) $x = 0.1$ (b) $x = 0.05$, (c) $x = 0.02$ and (d) $x = 0.0005$. We set $T = 40$ MHz and $E_C = 300$ MHz. The Josephson energies ($E_{J,1} = 98.8$ GHz and $E_{J,2} = 101.2$ GHz) lie above the experimentally relevant parameter range.

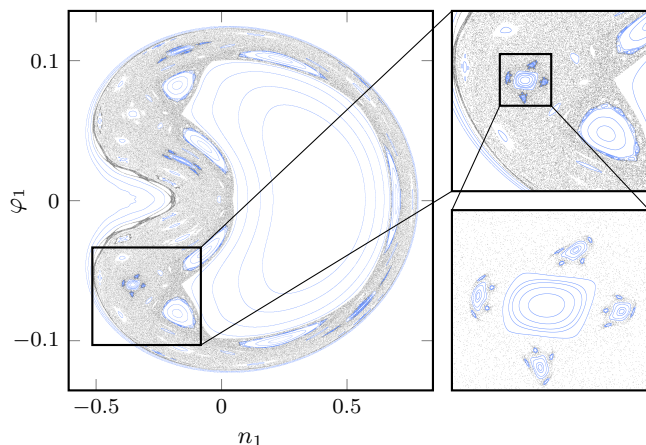


FIG. 3. Signatures of nonlinear dynamics in a system of two coupled transmons. Parameters are chosen as in Fig. 2(c). The figures represent orbits with identical energy but different initial conditions, leading to integrable (blue) or chaotic (gray) dynamics. Note the self-similar structure of orbits and satellite orbits upon magnification.

phase space contains integrable and chaotic regions. Examples of these include Kolmogorov-Arnold-Moser (KAM) tori [41], the intermittent presence of elliptic and hyperbolic fixed points required by the Poincaré-Birkhoff theorem (see, e.g., Ref. [42]), and self-similarity.

While the above analysis is proof of principle of the presence of chaos in the two-transmon system, it is of no practi-

cal relevance: The energies where the onset of chaos is observed lie well beyond those relevant for computing applications, i.e., the energies corresponding to the computational states $|00\rangle, |10\rangle, |11\rangle$ according to the mapping discussed in the previous section. However, as we are going to show next, the situation changes dramatically when we pass from two- to many-transmon arrays.

B. Ten coupled transmons

As a first step towards understanding the physics of many-transmon arrays, we now discuss a model of $L = 10$ transmons coupled in a chain geometry, for energies pertinent to quantum computing applications. More precisely, the system is prepared in the $|1010\dots\rangle$ state, i.e., the angles φ_i on the even (odd) sites are chosen such that the initial single transmon energies correspond to the quantum mechanical energies E_0 (E_1). To diagnose chaos, we calculate the maximal Lyapunov exponent λ , i.e., the rate at which trajectories with initial phase space distance $\delta\pi$ diverge, i.e., $\delta\pi(t) \approx \delta\pi \exp(\lambda t)$, for more details, see Appendix 1.

Fig. 4(a) shows the results as a function of the Josephson energy E_J and the coupling T , averaged over a large number of ‘disorder’ configurations. Each of these instances is generated by the independent drawing of ten values $E_{J,i}$ from a normal distribution with mean E_J and standard deviation $\delta E_J = \sqrt{E_J E_C}/8$. As detailed in Appendix 2, this peculiar choice for δE_J ensures a constant frequency disorder (as E_J varies) of $\delta\nu_q \approx \frac{E_C}{2}$ akin to what is found for current-

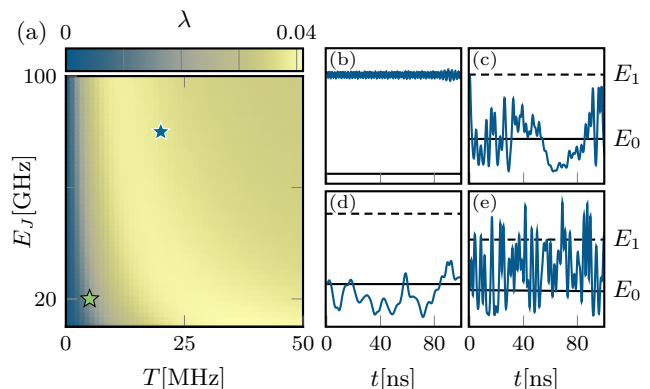


FIG. 4. Classical chaos in a chain of ten coupled transmons. (a) The maximal Lyapunov exponent in the (E_J, T) plane averaged over at least 8,000 disorder realizations. (b)–(e) Time-dependent single transmon energies for the sites 5 (upper row) and 6 (lower row) for two disorder realizations. The left (right) column corresponds to the parameters marked by the green (blue) star in (a). Whereas the Hamilton functions remain near their initial values in (b) and (d), they fluctuate heavily on timescales much shorter than typical decoherence times in (c) and (e). Only in the first case can one draw a credible conclusion that the initial bitstring is ‘1010...’ from the energies at $t > 0$. This consideration shows that the magnitude of λ , which is small for (b) and (d) but large for (c) and (e), can serve as a quality indicator of the classical transmon ‘storage device’.

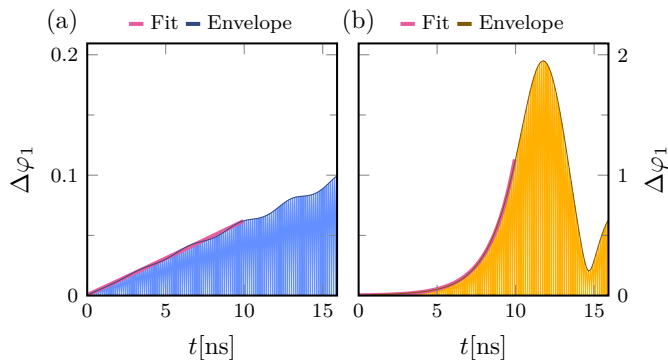


FIG. 5. **Divergence of classical trajectories.** Shown is the difference $\Delta\varphi_1$ between the angular coordinates of the first qubit in a 10-qubit chain for two trajectories initialized with a starting mismatch $\varphi'_1(0) = 1.001\varphi_1(0)$. The two trajectories are initialized to mimic a $|1010101010\rangle$ quantum state via their angular displacement. System parameters: (a) $T = 5$ MHz, $\delta E_J = 0.5$ GHz, (b) $T = 10$ MHz, $\delta E_J = 0.1$ GHz, and in both cases $E_C = 250$ MHz and $E_J \approx 10$ GHz. The magenta lines show exponential fits to the envelopes of $\Delta\varphi_1$. For (a) the fit stretches out to a linear function, while for (b) the fit gives a strong exponential growth of $\Delta\varphi_1$. The corresponding maximal Lyapunov exponents are (a) $\lambda \approx 0$ and (b) $\lambda \approx 0.03$.

generation quantum processors.

The omnipresence of chaos for experimentally relevant parameter values reveals itself in a non-vanishing Lyapunov exponent for almost the entire phase diagram of Fig. 4(a). The exception to the rule is a narrow region near $T = 0$, the limit of uncoupled pendula. Increasing T leads to a sharp increase of the Lyapunov exponent towards a maximum value, and finally the levelling at a value slightly below that maximum. Fig. 6 shows this behavior of the T -dependent Lyapunov exponent, now plotted as a function of the scaling variable $T\sqrt{E_J}$ for different values of E_J . The observation here is that under this rescaling, the two parameter function $\lambda(T, E_J) \rightarrow \lambda(T\sqrt{E_J})$ shows data collapse, indicating that $T\sqrt{E_J}$ is the relevant parameter controlling the onset of (quantum) chaos. We will return to this point when we discuss the quantum interpretation of our classical findings in the next section.

To develop some intuition for the meaning of a non-vanishing Lyapunov exponent, Fig. 5 exemplifies the sensitivity to variations in initial conditions (a mismatch of 0.1% in the first angular coordinate of a 10 transmon array) for realistic system parameters. While for $\lambda = 0$ (left) the initial mismatch increases linearly, we observe exponential behavior on a scale magnified by one order of magnitude for $\lambda \approx 0.03$, which eventually gives way to aperiodic fluctuations due to the compact range of the angular parameter space.

What are the implications of these findings for the application of the transmon array as an information processing device? Specifically, the reliable storage of information requires that a qubit initialized in either of the computational states $|0\rangle$ or $|1\rangle$ maintains this state under the evolution governed by the time independent Hamiltonian Eq. (3). In the classical reading, this situation corresponds to a transmon initialized in one

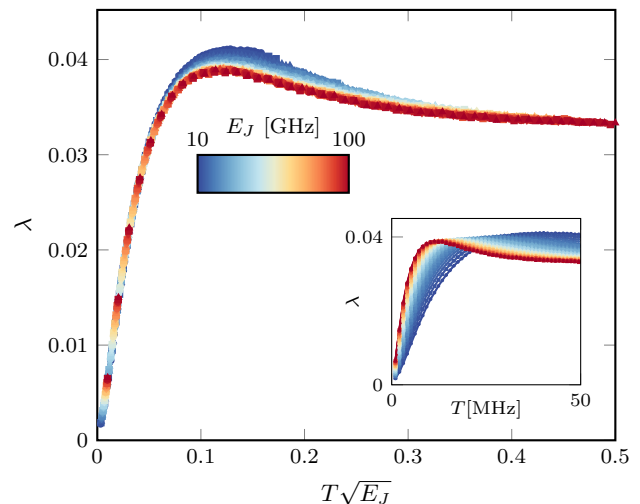


FIG. 6. **Data collapse for the maximal Lyapunov exponent.** Lyapunov exponent plotted for different values of E_J as a function of T (inset) and of the scaling variable $T\sqrt{E_J}$ main panel. In the latter case the data collapses almost perfectly for small T and still reasonably well for larger values: $T\sqrt{E_J}$ is the relevant parameter controlling the onset of chaos.

of the energies $E_{0,1}$ matching the qubit energies. The maintenance of the state translates to the condition that the time dependent energy $E_i(t) = H_i(t)$, i.e., the instantaneous value of the i th transmon's Hamilton function, remain close to its initial value. (We note that the total energy of the array is dynamically conserved, but that of its constituent transmons is not.) At the very least, it should not cross E_0 if initialized in E_1 and vice versa.

Panels Fig. 4 (b), (c), and (d), (e) show the energies E_5 and E_6 , respectively, for an array initialized in a configuration with energies (E_1, E_0, E_1, \dots) corresponding to the quantum state $|1, 0, 1, \dots\rangle$. The left and right panels correspond to parameter values marked by a green and blue star in panel (a). We observe that for near-integrable dynamics (green), the initial energies $E_5(0) = E_1$ and $E_6(0) = E_0$ remain approximately conserved. In the chaotic case (blue), however, there are erratic fluctuations, exceeding the energy spacing $E_1 - E_0$. These fluctuations build up after a few nanoseconds, far shorter than characteristic qubit coherence times. We conjecture, and will discuss in more detail below, that in this regime the functioning of the storage is compromised.

Fig. 7 (a) shows the generalization of the Lyapunov data to different transmon configurations. In the main panel, we plot λ for a variety of (classical analogs of) computational states. The data shows a general trend towards larger Lyapunov exponents for increasing state energy, i.e., larger numbers of $E_1 \leftrightarrow |1\rangle$ initializations. All curves exhibit the same qualitative behavior as a function of T as that discussed above, the reaching of a maximum value followed by saturation. Panel (b) shows data for states, (E_a, E_0, E_a, \dots) , with $a = 0, 1, 2, 3$. (The generalization to non-computational states, $a > 1$, is practically relevant as transmon gate operations transiently couple to states outside the computational

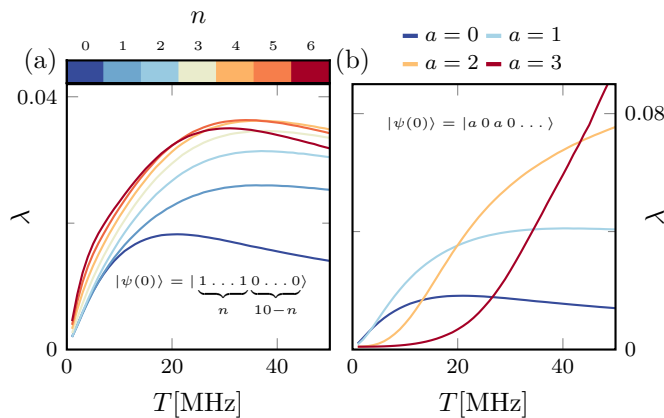


FIG. 7. **Influence of the state energy on the dynamics.** (a) Lyapunov exponents for computational states of increasing energy. (b) Lyapunov exponents for configurations including transmons initialized in states $E_{0,1,2,3}$ including values outside the computational sector. Values given are from a 10 qubit transmon chain with $E_C = 250$ MHz, $E_J = 10$ GHz, and $\delta E_J = 559$ MHz. Each point is the mean value of 20,000 disorder realizations. For discussion, see text.

sector [43].) Two features stand out: The Lyapunov exponents reach (i) larger values, however, these maximal values are attained (ii) only for larger values of the coupling. We reason that the relatively higher inertia to changes in T has to do with the fact that for larger energies of individual transmons the coupling represents a relatively weaker perturbation. We note that these findings are consistent with a recent study [44] of a (quantum) Bose-Hubbard model, that finds a suppression of the effective interaction between states with large occupation numbers on individual transmon sites.

IV. PREDICTIVE POWER OF CLASSICAL SIMULATIONS

At this point, we have discussed key signatures of the classical dynamics of small scale transmon arrays. The big question now of course is what bearings these findings have for our actual subject of interest, the quantum processor. In this section, we formulate an answer in a succession of steps. First, as a warmup, we show that several of the observations of the previous section afford a quantum interpretation. We then compare our results above with those of quantum simulations for the ten transmon array, and for identical material parameters (except that now $\hbar \neq 0$, of course), to observe a high level of agreement: classical chaos implies quantum chaos, and vice versa. We finally turn to the trump card of the classical approach, namely the option to reliably simulate arrays of thousands of transmons. Assuming that the quantum-to-classical fidelity extends to large numbers, we thus have a tool to obtain stability measures for realistic quantum hardware outside the reach of quantum simulation on classical computers. In section V, we substantiate this point by simulating large scale two-dimensional transmon arrays of current IBM design.

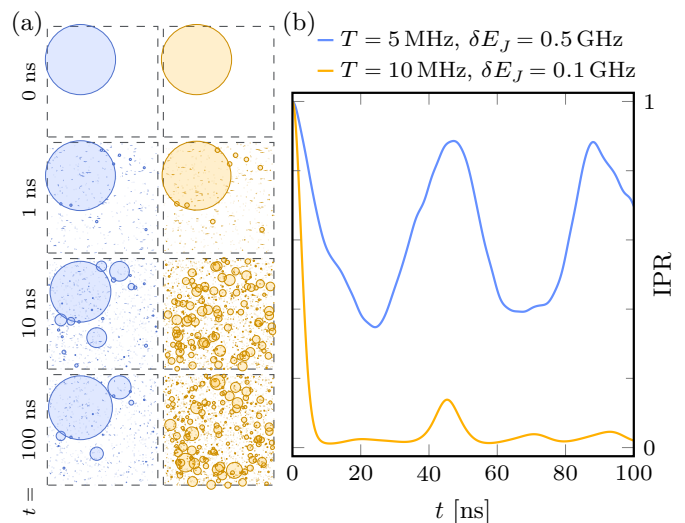


FIG. 8. **Visualization of Fock space state fragmentation** in the time evolution, $|\psi(t)\rangle$, of a state initialized as $|\psi(0)\rangle = |1010\dots\rangle$, i.e. the quantum state corresponding to the classical initial condition considered in Fig. 5. The system parameters, E_J , E_C , T , too, are those previously used in Fig. 5 (a), blue, integrable and (b), yellow, chaotic. (a) Circles are centered around randomly chosen assignments of occupation number states to coordinates in the plane, and their areas quantify the probability to find $|\psi(t)\rangle$ in these states. The four rows illustrate how the integrable (chaotic) state retains its structure (fragments) in a succession of four discrete time steps. (b) The continuous time evolution of the inverse participation ratio of $|\psi(t)\rangle$.

A. Quantum to classical correspondence (qualitative)

Quantum mechanically, the passage from integrable to chaotic dynamics upon increasing T is a manifestation of a Fock space (de)localization transition: In the transmon regime, $E_J \gg E_C$, Eq. (3) is well approximated by the attractive Bose-Hubbard model [45]. Thinking of the Fock basis, defined by the occupation numbers of the transmons (n_1, n_2, \dots, n_L) , as a lattice whose sites are connected through the capacitive interaction, one expects that wave functions delocalize if the hopping amplitude t between these lattice sites is larger than the ‘on-site’ (in Fock space) energy difference $\Delta\epsilon$. In terms of the transmon array parameters, the hopping amplitude reads $t = T\sqrt{E_J}/\sqrt{32E_C}$ [4, 7]. The many-body level spacing depends on the total anharmonicity of the Fock space lattice sites and the disorder in the qubit frequencies. In our simulations, both contributions are proportional to E_C and independent of E_J , see Appendix 2, i.e., $\Delta\epsilon \propto E_C$. For the scaling variable, this yields $\frac{t}{\Delta\epsilon} \propto T\sqrt{E_J}/\sqrt{E_C^3}$. Since E_C is kept constant in the simulations, one expects that the contour lines separating regimes of (integrable) many-body localized and extended chaotic regimes, scale as $\frac{t}{\Delta\epsilon} \propto T\sqrt{E_J} = \text{const}$. Below, we will demonstrate this scaling for the system’s wave function statistics. The finding that the classical Lyapunov exponents scaled with the same parameter is consistent with the paradigm that quantum and classical chaos condition each other.

In the classical context, ‘delocalization’ is delocalization away from the integrable orbits of the oscillator motion of individual transmons. Quantum mechanically, it stands for the spreading of many body wave functions over a large set of occupation number sites. To illustrate this phenomenon, we consider the quantum evolution of the states corresponding to the classical initial conditions discussed in connection with Fig. 5. The resulting Fock space structure is visualized in Fig. 8 (a), where the circles are centered around an arbitrary mapping of Fock space sites of total occupation number 5 (e.g. $|01130\dots\rangle$) to the two-dimensional plane, and circle areas quantify the square amplitude of the states at these sites. The left (right) panels map four stages in the time evolution of an initial state with parameters previously used in the left (right) panel of the classical Fig. 5. We observe that a vanishing (large) Lyapunov exponent corresponds to approximate state stationarity (fragmentation) in the quantum system. In the following, we discuss inverse participation ratios as a means to quantify these structures.

B. Quantum to classical correspondence (quantitative)

In the following, we consider the wave function inverse participation ratio (IPR) as a sensitive measure of quantum chaotic dynamics [46]. For a many-body wave function $|\psi\rangle$, this quantity is defined as

$$\text{IPR} = \sum_k |\langle k|\psi\rangle|^4, \quad (8)$$

where the sum is over the Fock state basis. The limiting cases to be distinguished are $\text{IPR} \approx 1$ indicating localization in the k -basis, and $\text{IPR} = 1/\dim \mathcal{H}$ for chaotic states ergodically spread over Hilbert space [23].

The bottom left panel of Fig. 9 color-codes the IPR for the ten transmon quantum array in the occupation number eigenbasis of the $T = 0$ system, where dark blue and bright yellow encode the above limiting cases of localization and ergodicity, respectively. The upper left panel shows the previously computed Lyapunov exponents in the same representation. The two measures evidently show similar behavior as a function of the material parameters. In particular, the lines of constant IPR/λ both follow the parametric $E_J \propto 1/\sqrt{T}$ dependence, as discussed above.

The remaining panels extend this comparison to larger values of the disorder, from the ‘natural disorder’ in the left column, as also discussed in Fig. 4, to about ten times larger disorder, $\delta\nu_q > 1$ GHz, realized, e.g., in recent flux-tunable architectures [13]. The main point here is that, at first counter-intuitively, disorder may support integrable dynamics: Upon increasing disorder the chaotic regions retract and eventually vanish. The physics behind this observation is that increasing disorder means a diminished susceptibility for the transmons to be driven into a chaotically resonant regime by transmon coupling.

We finally remark that the presence of a shallow maximum of the classical Lyapunov exponent at intermediate T observed in the last section is consistent with the proposal

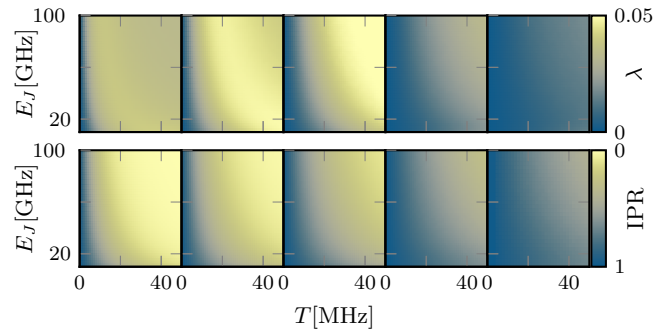


FIG. 9. **Quantum to classical correspondence.** Comparison of the classical and the quantum dynamics of ten coupled transmon oscillators, averaged over at least 3,000 realizations of disorder of increasing strength $\delta\nu_q = c \cdot E_C$ with (left to right), $c = 1/2$ (as in Fig. 4), $c = 1$, $c = 2$, $c = 4$, $c = 6$. The desired frequency disorder is realized by scaling $\delta E_J \propto \sqrt{E_J}$, as discussed in Appendix 2. For the classical simulation, the system is initialized in the (E_1, E_0, E_1, \dots) , in the quantum case, the IPR is averaged over states with total Fock space occupation number $L/2$.

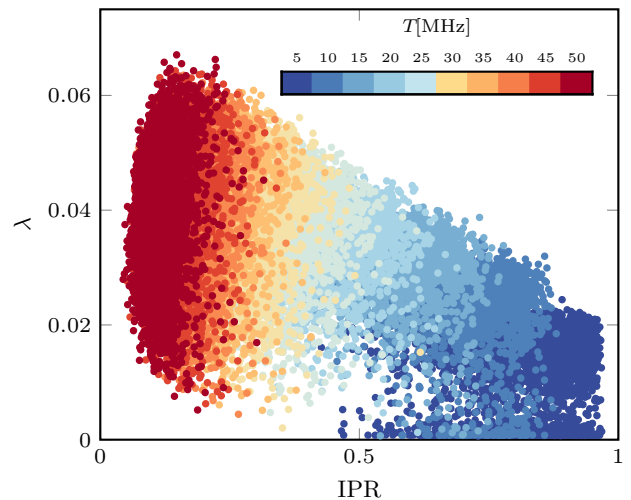


FIG. 10. **Correlation plot of maximal Lyapunov exponent and IPR.** Each of the dot represents one individual disorder realization for a 10 qubit transmon chain for different coupling strengths (indicated by the colors). The figure contains 2,000 data points per coupling strength. We set $E_J = 12.5$ GHz and $E_C = 250$ MHz. The IPRs are averaged over all relevant wave functions, as explained in Fig. 9.

[47] of a domain of *maximal chaos* in-between the localized and the ergodic regime. The statement is that in transit from integrable to chaotic phases one passes a regime with exponentially enhanced eigenvector susceptibility. Eigenstates in this intermediate terrain, although not yet fully extended over Hilbert space, show higher sensitivity to perturbations than in the ‘usual’ ergodic quantum chaotic phase. This behavior may be the quantum manifestation of an intermediate regime of exceptional classical Lyapunov sensitivity.

The above discussion qualitatively demonstrates quantum-to-classical correspondence in the parameter space

$(E_J, T, \delta E_J)$. However, ultimately, one would like to turn the classical analysis into a prognostic tool for, e.g., optimal quantum system parameters. To this end, the relationship between Lyapunov exponent and IPR – yardsticks for classical and quantum chaos, respectively – needs to be understood in quantitative terms. As a first attempt in this direction, Fig. 10 displays the correlations between the Lyapunov exponent and the IPR for coupling strengths stepwise increased between 5 and 50 MHz (color code). For each value, we explicitly show 2,000 distinct disorder realizations (each corresponding to a single point in the figure).

The take-home message of this analysis is that the relationship between the two quantifiers of chaos is statistical in nature. For example, a single shot numerical measurement of a small exponent $\lambda_{\max} = 0.02$ can be consistent with IPRs distributed almost over the full range, and hence is of not much predictive value. However, extreme value statistics applied to a large set of values of λ obtained for different disorder realizations does produce valuable information. The well developed linear bound visible in the figure implies a quantitative relation between the largest Lyapunov exponent of the ensemble and the expected maximal value of the IPR.

We further note that, with the exception of the smallest values of the coupling, the IPRs show lesser statistical variation than the Lyapunov exponents. This feature shows in the vertical stripe-like pattern visible in Fig. 10, and in an alternative representation in Fig. 11. That figure shows the distribution of the measured values of Lyapunov exponents (lower panel) and IPRs (upper panel). We observe that for large values of the coupling, the IPRs are comparatively narrowly distributed. For smaller values, the distribution widens, but even there remains benign in the sense that average value and width of the distribution are of the same order.

We conclude that knowledge of a distribution of Lyapunov exponents contains information on the spread of quantum wave functions over the transmon Hilbert space. It is probably safe to say that IPRs larger than $1/2$ are required to safeguard the integrity of quantum storages. (Current IBM efforts (see Section V) strive to reach values close to the optimal value unity.) Our analysis shows that, for all array realizations considered in this paper, this conservative estimate translates to the condition $\lambda < 0.04$. In practical terms, the need to harvest Lyapunov ensembles to establish these upper bounds for the IPR is not a big issue. As discussed in the next section the computation of exponents including for systems way beyond current NISQ era extensions is relatively effortless.

C. Simulation of large arrays

The discussion so far was formulated for an array of ten transmons, a system size comfortably in reach of both classical and quantum simulation (on classical computers). The computational cost of quantum simulations grows exponentially in system size, limiting it to system sizes of perhaps twice or thrice that value, but not much larger. Currently existing transmon hardware with 50-100 qubits can no longer be simulated on classical machines. Our discussion above un-

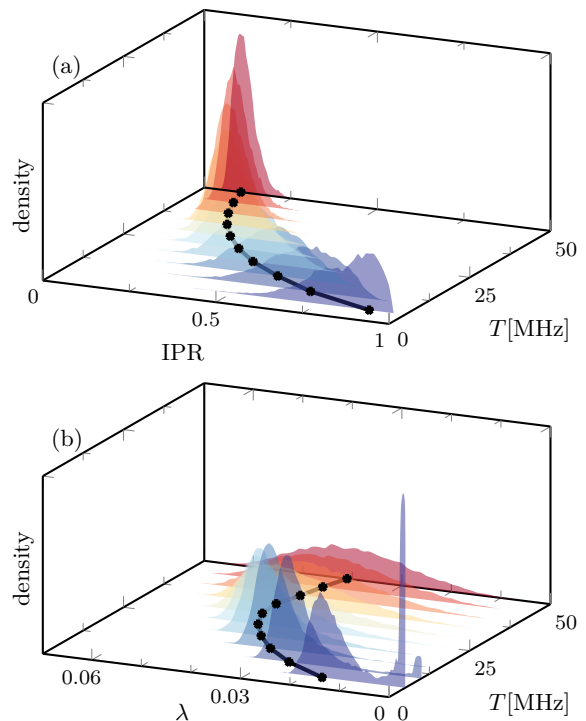


FIG. 11. Histograms of inverse participation ratio (a) and maximal Lyapunov exponent (b) of Fig. 10, for different coupling strengths. The black lines indicate the position of the peak maxima.

derpins that this may be an actual limitation. Tendencies to instability and chaos increase with system size (for more on this, see below), and conclusions drawn on the quantum simulation of a sub-unit of a transmon array may not fully capture the physics of the whole.

The computational cost of classical simulation, on the other hand, grows only linearly in size, implying that arrays up to and beyond current hardware designs are comfortably within reach. For more details on the algorithmic scaling and actual compute times of our classical simulations we refer to Appendix 3. Fig. 12 shows the disorder-averaged Lyapunov exponent λ for chain geometries between 2 and $2^{12} = 4,096$ transmons. We observe a tendency to more pronounced symptoms of classical chaos at larger system size. Beginning with the integrable (flat line) two-transmon arrays, the Lyapunov exponents show increasingly sharp increase at larger L . In the next section, we will apply the classical analysis to transmon architectures modeled after existing hardware layouts, including two-dimensional geometries.

V. STATE-OF-THE-ART TRANSMON CHIPS

We now move away from the linear transmon chains studied so far to two-dimensional geometries and, in particular, a selection of recently introduced processor generations. Our conclusions will include suggestions for future design modifications.

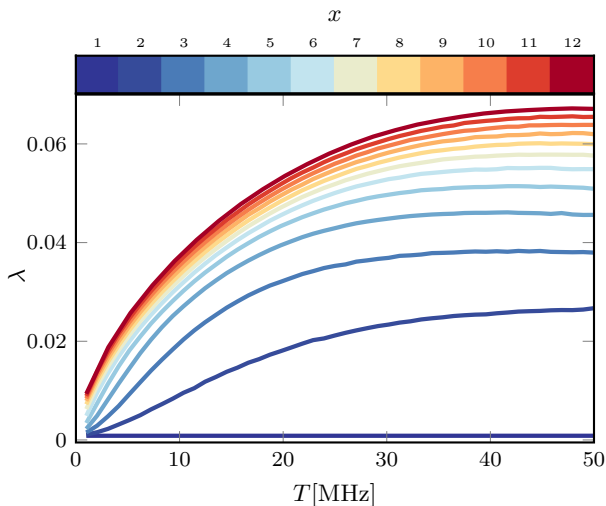


FIG. 12. **Classical chaos in chain geometries of varying length.** Lyapunov exponents for linear arrays of $L = 2^x$, $x = 1, \dots, 12$ transmons. ($E_J = 10$ GHz and disorder strength, $\delta\nu_q = \frac{E_C}{2}$, the arrays are initialized in the $|E_1, E_0, E_1, \dots\rangle$ state.) The number of disorder realizations varies from 2,000 ($x = 12$) to 20,000 ($x = 1-6$).

A. Large-scale IBM transmon chips

We study classical transmon dynamics on the *heavy-hexagon lattice*, a design proposed by IBM as advantageous when upscaling the number of qubits in cross-resonance architectures [12, 24]. Its layout consists of a hexagonal qubit lattice with an additional transmon on each edge, as shown in Fig. 13. (The cross-resonance two-qubit gate involves a target and a control qubit whose correlation is microwave activated. The above geometry with target qubits at nodes connected via control qubits on the links of the lattice is tailored to this design principle.) The colored segments illustrate the evolution of IBM’s processor families according to their quantum roadmap [25], from Falcon (27 qubits, introduced in 2019) to the 1,121-qubit Condor chip (to be introduced in 2023).

The main difference compared with our previous analysis is that now we are considering a two-dimensional geometry with a higher transmon connectivity (which in our simulations, however, does not imply a serious setback in computational reach). We use the same Gaussian disorder distribution as before, and choose initial configurations of intermediate energy density within the computational subspace. To be specific, we will monitor the fate of two initial states, one with all control qubits initialized in E_1 and targets in E_0 , the other one with exchanged roles $E_0 \leftrightarrow E_1$. Since there are more control than target qubits (asymptotically by a factor 3/2), we refer to the former (latter) as the high- E (low- E) configuration.

In Fig. 14, we compare the Lyapunov exponent for these two distinct density patterns for (a) the Falcon and (b) the Hummingbird layout and three different values of the Josephson energy E_J . The data shows many commonalities with that of the chain geometry: single parameter scaling in the vari-

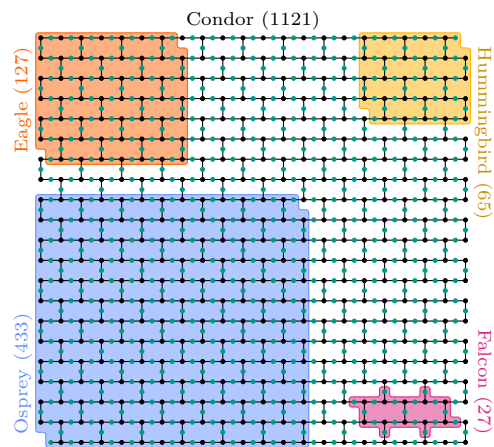


FIG. 13. **Heavy-hexagon geometry and IBM processors.** A 1,121-transmon heavy hexagon layout with control (green) and target (black) qubits. The colored cut-outs indicate the growth of IBM’s monolithic processor families, starting with the 27-qubits Falcon (pink, introduced in 2019), continued by Hummingbird (yellow, 65 qubits, 2020), Eagle (orange, 127 qubits, 2021), and Osprey (blue, 433 qubits, 2022), and Condor (entire lattice, 1,121 qubits, announced for 2023).

able $T\sqrt{E_J}$, a steep increase towards a maximum, followed by a gradual diminishing towards a plateau value, and larger chaotic instability for states of higher energy. The Lyapunov exponents of the two processors are similar. Both are larger by about 30% than those of the linear geometry, i.e., the extension to two dimensions leads to a noticeable, but not dramatic increase in chaoticity. The earlier reaching of threshold values such as $\lambda \simeq 0.04$ implies that for larger chips one may need to work with smaller inter-transmon coupling to guarantee stability.

In Fig. 15, we extend the analysis to all monolithic IBM processors and show λ as a function of the coupling T for each of the geometries shown in Fig. 13, and for the arrays

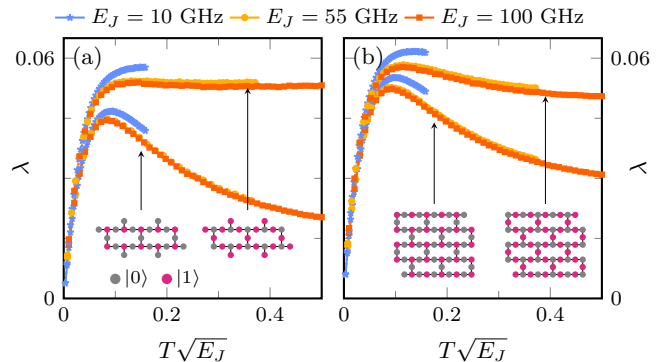


FIG. 14. **Lyapunov exponents of Falcon and Hummingbird processors.** Shown is a disorder-averaged Lyapunov exponent λ for (a) the Falcon and (b) the Hummingbird processor geometry, respectively. Data is for three different values of E_J , and states initialized in the high (solid) and low (dotted) energy configuration. ($E_C = 250$ MHz.)

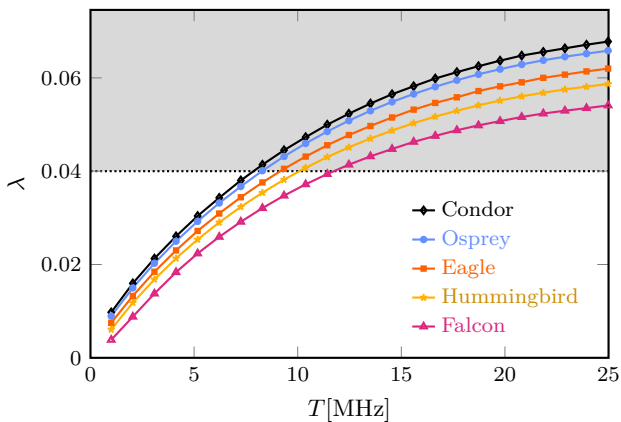


FIG. 15. **Classical chaos in IBM quantum processors.** Lyapunov exponents of states initialized in the high- E configuration averaged over ~ 700 (Condor) to $\sim 15,000$ (Falcon) realizations for all layouts shown in Fig. 13. ($E_J = 10$ GHz and $E_C = 250$ MHz.)

initialized in the high- E state. (The data for low- E initialization looks qualitatively similar.) The tendency towards dynamic instabilities rises with the total number of qubits in the chip, e.g. the threshold value of $\lambda = 0.04$ (indicated by the dotted line) is reached for smaller inter-transmon coupling T with increasing chip size, decreasing by about a factor of two between the Falcon and Condor chips. This calls for additional engineering efforts to avoid chaotic instabilities in larger transmon chips.

B. Frequency-engineered transmon arrays

The fidelity of cross-resonance processor layouts may be increased by introducing engineered frequency patterns via the recently introduced laser-annealing technique (LASIQ) [12]. The idea behind such patterning is similar to that of engineered disorder. A detuning of neighboring qubit frequencies avoids degeneracies – so-called frequency collisions – and their unwanted resonance effects. However, there needs to remain a residual random frequency spread (see Ref. 7 for details), the reason being that in a perfectly engineered A - B - A - B pattern, the blocking of A - B degeneracies would come at the price of a perfectly realized resonance between next-next-neighbor A - A 's and B - B 's. Some degree of frequency variation is required to prevent these next-nearest-neighbor resonances. We are thus led to investigate a situation with weak disorder on top of a regularly patterned background.

In Ref. [7], some of us considered the many-body physics of a toy model of a 3×3 transmon array subject to A - B sublattice patterning. In a nutshell, the combined effect of an order-of-magnitude reduction of disorder and the A - B patterning leads to a restructuring of the Hilbert space into smaller subspaces, denoted as *permutation multiplets*. Individual multiplets harbor all Fock spaces of a definite distribution of occupations on the two sublattices. For example, $\{A11B111\}$ is the forty-dimensional multiplet defined by all states with two A sites and three B sites in state $|1\rangle$ all others in $|0\rangle$. Multi-

plets are energetically separated by energy scales defining the underlying A - B substructure. The intra-multiplet state structure is determined by the degree of residual disorder: from Bloch state extended (asymptotically weak disorder), over chaotically extended (weak disorder) and intra multiplet Fock space localized (moderate disorder), to random hybridization between multiplets (strong disorder), see Ref. [7].

IBM transmon engineering has managed to hit the sweet spot of intra-multiplet state localization, visible as a local maximum in the IPRs shown in the right panel of Fig. 16, where the four alternating vertical strips represent the regimes of increasing disorder mentioned above. The colors represent multiplets of Hilbert space dimension between 1 and 60 defined by the different excitation patterns indicated in the legend. The $\text{IPR} \approx 1$ indicates a high level of state definition for all multiplets at intermediate disorder.

The left panel shows that the Lyapunov exponents of this system (in its classical limit) do not fully reveal the quantum mechanical state structure. However, they still define a useful diagnostic tool. Upon increasing disorder, the Lyapunov exponents remain structureless up until the point where the optimal disorder concentration is reached. Pragmatically, one may thus gather evidence on the preferred level of randomness by running a Lyapunov analysis for a variety of multiplet occupation patterns.

Following the general strategy of this paper, we have pushed this analysis to system sizes beyond the reach of quantum simulation. Fig. 17 shows data for a 54-qubit C - A - C - B patterned Hummingbird chip with 37 transmons initialized in E_1 , and the remaining ones in E_0 . The blue line shows the Lyapunov exponents for the specific initial condition where the 37 excited transmons are the 37 C 's, i.e. a configuration corresponding to a one-dimensional quantum multiplet. We

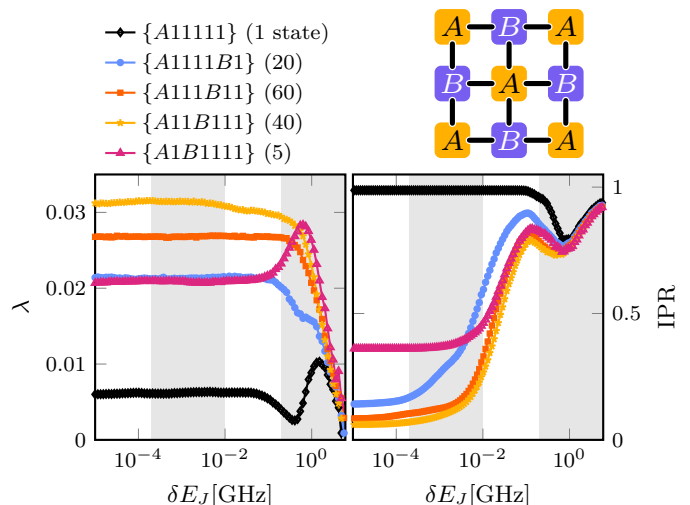


FIG. 16. **State localization in precision engineered transmon arrays** Lyapunov exponents (left) and IPRs (right) of computational multiplets in a nine qubit AB patterned transmon array averaged over 8000 realizations of disorder. ($E_{J,A} = 12.58$ GHz, $E_{J,B} = 13.80$ GHz, $E_C = 330$ MHz [12] and $T = 6$ MHz.)

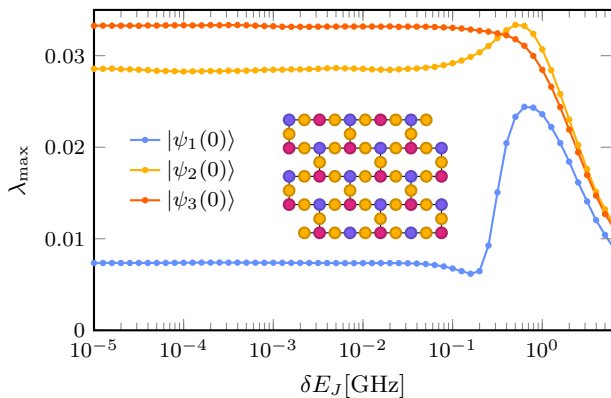


FIG. 17. **Classical chaos in frequency-engineered Hummingbird chips.** Lyapunov exponents of the C - A - C - B patterned Hummingbird chip, with 37 (17) transmons in the E_1 (E_0) state. (Adopting IBM parameters, we set $E_C = 330$ MHz, and $E_J = (11.05, 11.33, 10.76)$ GHz for transmons on the (A, B, C) sites. The coupling is set to $T = 6$ MHz and all results are averaged over 20,000 disorder realizations.

observe structural similarity to the one-dimensional configuration shown in Fig. 16, and similarly low-lying Lyapunov exponents. For the other configurations, with random distribution of the excited transmons, the exponents assume larger values. There is a gradual tendency to increased chaoticity compared to that of the smaller system, following the general trend observed in this paper. Finally, the more elaborate three-frequency patterning does not appear to have a positive effect on the stability of the system.

VI. SUMMARY

In this paper we have proposed simulations in the classical limit $\hbar \rightarrow 0$, but otherwise realistic system parameters, as a potent benchmarking tool for the resilience of transmon-based superconductor quantum information hardware against chaotic instability. Our analysis proceeded in a succession of four conceptual steps: 1) the demonstration of classical chaos

even in small-sized arrays and energies relevant to quantum computation, 2) the construction of a correspondence showing that classical chaos evidenced by finite Lyapunov exponents implies quantum chaos evidenced by decreasing wave function participation ratios, and the extension of this correspondence to a quantitative tool, 3) the demonstration that classical simulation is feasible for array sizes well beyond current hardware limits (and orders of magnitude beyond the reach of quantum simulations), and 4) application of this toolbox to layouts modelled after current IBM chip designs.

The overall conclusion of this analysis is that the current engineering of frequency-patterned transmon arrays operates in a comparatively narrow corridor between insufficient and dangerously resonant coupling. We observe a tendency to growing instability for larger arrays, and for growing energy of computational states (more $|1\rangle$'s than $|0\rangle$'s.) To fully understand the potential ramifications of chaos in this setting, it may be necessary to extend the analysis from time independent signatures of wave functions to dynamical protocols describing multi-qubit structures in operation. Simulating the corresponding non-autonomous classical dynamical system will be a subject of future research. We finally remark that additional hardware overhead, such as tunable couplers, appears to provide lasting immunization against the effects discussed in this paper.

ACKNOWLEDGMENTS

We thank E. Varvelis for discussions and P. Bönninghaus for collaboration on an initial project [48] studying incipient chaos in large-scale classical transmon systems. We acknowledge partial support from the Deutsche Forschungsgemeinschaft (DFG) under Germany's Excellence Strategy Cluster of Excellence Matter and Light for Quantum Computing (ML4Q) EXC 2004/1 390534769 (D.P.D., S.T., and A.A.) and within the CRC network TR 183 (project grant 277101999) as part of projects A04 and C05 (S.-D.B., C.B., S.T., and A.A.). The numerical simulations were performed on the JUWELS cluster at the Forschungszentrum Jülich.

[1] M. Tabor, *Chaos and Integrability in Nonlinear Dynamics: An Introduction* (Wiley, 1989).
 [2] J. Koch, T. M. Yu, J. Gambetta, A. A. Houck, D. I. Schuster, J. Majer, A. Blais, M. H. Devoret, S. M. Girvin, and R. J. Schoelkopf, Charge-insensitive qubit design derived from the Cooper pair box, *Phys. Rev. A* **76**, 042319 (2007).
 [3] P. Krantz, M. Kjaergaard, F. Yan, T. P. Orlando, S. Gustavsson, and W. D. Oliver, A quantum engineer's guide to superconducting qubits, *Applied Physics Reviews* **6**, 021318 (2019).
 [4] A. Blais, A. L. Grimsmo, S. M. Girvin, and A. Wallraff, Circuit quantum electrodynamics, *Reviews of Modern Physics* **93**, 025005 (2021).
 [5] M. Kjaergaard, M. E. Schwartz, J. Braumüller, P. Krantz, J. I.-J. Wang, S. Gustavsson, and W. D. Oliver, Superconducting

Qubits: Current State of Play, *Annual Review of Condensed Matter Physics* **11**, 369 (2020).
 [6] T. Orell, A. A. Michailidis, M. Serbyn, and M. Silveri, Probing many-body localization phase transition with superconducting circuits, *Phys. Rev. B* **100**, 134504 (2019).
 [7] C. Berke, E. Varvelis, S. Trebst, A. Altland, and D. P. DiVincenzo, Transmon platform for quantum computing challenged by chaotic fluctuations, *Nature Communications* **13**, 2495 (2022).
 [8] F. Yan, P. Krantz, Y. Sung, M. Kjaergaard, D. L. Campbell, T. P. Orlando, S. Gustavsson, and W. D. Oliver, Tunable Coupling Scheme for Implementing High-Fidelity Two-Qubit Gates, *Phys. Rev. Applied* **10**, 054062 (2018).

- [9] Y. Xu, J. Chu, J. Yuan, J. Qiu, Y. Zhou, L. Zhang, X. Tan, Y. Yu, S. Liu, J. Li, F. Yan, and D. Yu, High-Fidelity, High-Scalability Two-Qubit Gate Scheme for Superconducting Qubits, *Phys. Rev. Lett.* **125**, 240503 (2020).
- [10] Y. Chen, C. Neill, P. Roushan, N. Leung, M. Fang, R. Barends, J. Kelly, B. Campbell, Z. Chen, B. Chiaro, A. Dunsworth, E. Jeffrey, A. Megrant, J. Mutus, P. O'Malley, C. Quintana, D. Sank, A. Vainsencher, J. Wenner, T. White, M. R. Geller, A. Cleland, and J. M. Martinis, Qubit Architecture with High Coherence and Fast Tunable Coupling, *Phys. Rev. Lett.* **113**, 220502 (2014).
- [11] F. Arute, K. Arya, R. Babbush, D. Bacon, J. C. Bardin, R. Barends, R. Biswas, S. Boixo, F. G. S. L. Brandao, D. A. Buell, B. Burkett, Y. Chen, Z. Chen, B. Chiaro, R. Collins, W. Courtney, A. Dunsworth, E. Farhi, B. Foxen, A. Fowler, C. Gidney, M. Giustina, R. Graff, K. Guerin, S. Habegger, M. P. Harrigan, M. J. Hartmann, A. Ho, M. Hoffmann, T. Huang, T. S. Humble, S. V. Isakov, E. Jeffrey, Z. Jiang, D. Kafri, K. Kechedzhi, J. Kelly, P. V. Klimov, S. Knysh, A. Korotkov, F. Kostritsa, D. Landhuis, M. Lindmark, E. Lucero, D. Lyakh, S. Mandrà, J. R. McClean, M. McEwen, A. Megrant, X. Mi, K. Michielsen, M. Mohseni, J. Mutus, O. Naaman, M. Neeley, C. Neill, M. Y. Niu, E. Ostby, A. Petukhov, J. C. Platt, C. Quintana, E. G. Rieffel, P. Roushan, N. C. Rubin, D. Sank, K. J. Satzinger, V. Smelyanskiy, K. J. Sung, M. D. Trevithick, A. Vainsencher, B. Villalonga, T. White, Z. J. Yao, P. Yeh, A. Zalcman, H. Neven, and J. M. Martinis, Quantum supremacy using a programmable superconducting processor, *Nature* **574**, 505 (2019).
- [12] J. B. Hertzberg, E. J. Zhang, S. Rosenblatt, E. Magesan, J. A. Smolin, J.-B. Yau, V. P. Adiga, M. Sandberg, M. Brink, J. M. Chow, and J. S. Orcutt, Laser-Annealing Josephson Junctions for Yielding Scaled-up Superconducting Quantum Processors, *npj Quantum Information* **7**, 1 (2021).
- [13] S. Krinner, N. Lacroix, A. Remm, A. Di Paolo, E. Genois, C. Leroux, C. Hellings, S. Lazar, F. Swiadek, J. Herrmann, G. J. Norris, C. K. Andersen, M. Müller, A. Blais, C. Eichler, and A. Wallraff, Realizing Repeated Quantum Error Correction in a Distance-Three Surface Code, *Nature* **605**, 669 (2022).
- [14] R. Versluis, S. Poletto, N. Khammassi, B. Tarasinski, N. Haider, D. Michalak, A. Bruno, K. Bertels, and L. DiCarlo, Scalable Quantum Circuit and Control for a Superconducting Surface Code, *Phys. Rev. Applied* **8**, 034021 (2017).
- [15] D. A. Huse, R. Nandkishore, and V. Oganesyan, Phenomenology of fully many-body-localized systems, *Phys. Rev. B* **90**, 174202 (2014).
- [16] D. A. Abanin, E. Altman, I. Bloch, and M. Serbyn, Colloquium: Many-body localization, thermalization, and entanglement, *Reviews of Modern Physics* **91**, 021001 (2019).
- [17] J. Cohen, A. Petrescu, R. Shillito, and A. Blais, Reminiscence of classical chaos in driven transmons, *PRX Quantum* **4**, 020312 (2023).
- [18] <https://www.ibm.com/quantum-computing/>.
- [19] E. J. Zhang, S. Srinivasan, N. Sundaresan, D. F. Bogorin, Y. Martin, J. B. Hertzberg, J. Timmerwilke, E. J. Pritchett, J.-B. Yau, C. Wang, W. Landers, E. P. Lewandowski, A. Narasgond, S. Rosenblatt, G. A. Keefe, I. Lauer, M. B. Rothwell, D. T. McClure, O. E. Dial, J. S. Orcutt, M. Brink, and Jerry M. Chow, High-Performance Superconducting Quantum Processors via Laser Annealing of Transmon Qubits, *Science Advances* **8**, eabi6690 (2022), <https://www.science.org/doi/pdf/10.1126/sciadv.abi6690>.
- [20] I. Pietikäinen, S. Danilin, K. S. Kumar, A. Vepsäläinen, D. S. Golubev, J. Tuorila, and G. S. Paraoanu, Observation of the bloch-siegert shift in a driven quantum-to-classical transition, *Phys. Rev. B* **96**, 020501 (2017).
- [21] I. Pietikäinen, J. Tuorila, D. S. Golubev, and G. S. Paraoanu, Photon blockade and the quantum-to-classical transition in the driven-dissipative josephson pendulum coupled to a resonator, *Phys. Rev. A* **99**, 063828 (2019).
- [22] The quantum simulations must include states outside the computational subspace that are fully intermingled with the qubit states [7, 43]. The simulations are therefore numerically costly, see also the discussion in Appendix 3.
- [23] F. Evers and A. D. Mirlin, Anderson transitions, *Rev. Mod. Phys.* **80**, 1355 (2008).
- [24] C. Chamberland, G. Zhu, T. J. Yoder, J. B. Hertzberg, and A. W. Cross, Topological and Subsystem Codes on Low-Degree Graphs with Flag Qubits, *Phys. Rev. X* **10**, 011022 (2020).
- [25] J. Gambetta, [Expanding the IBM Quantum Roadmap to anticipate the future of quantum-centric supercomputing](#) (2022).
- [26] C. Rigetti and M. Devoret, Fully Microwave-Tunable Universal Gates in Superconducting Qubits with Linear Couplings and Fixed Transition Frequencies, *Phys. Rev. B* **81**, 134507 (2010).
- [27] J. Preskill, Quantum Computing in the NISQ era and beyond, *Quantum* **2**, 79 (2018).
- [28] K. J. Satzinger, Y.-J. Liu, A. Smith, C. Knapp, M. Newman, C. Jones, Z. Chen, C. Quintana, X. Mi, A. Dunsworth, C. Gidney, I. Aleiner, F. Arute, K. Arya, J. Atalaya, R. Babbush, J. C. Bardin, R. Barends, J. Basso, A. Bengtsson, A. Bिल्mes, M. Broughton, B. B. Buckley, D. A. Buell, B. Burkett, N. Bushnell, B. Chiaro, R. Collins, W. Courtney, S. Demura, A. R. Derk, D. Eppens, C. Erickson, L. Faoro, E. Farhi, A. G. Fowler, B. Foxen, M. Giustina, A. Greene, J. A. Gross, M. P. Harrigan, S. D. Harrington, J. Hilton, S. Hong, T. Huang, W. J. Huggins, L. B. Ioffe, S. V. Isakov, E. Jeffrey, Z. Jiang, D. Kafri, K. Kechedzhi, T. Khattar, S. Kim, P. V. Klimov, A. N. Korotkov, F. Kostritsa, D. Landhuis, P. Laptev, A. Locharla, E. Lucero, O. Martin, J. R. McClean, M. McEwen, K. C. Miao, M. Mohseni, S. Montazeri, W. Mruczkiewicz, J. Mutus, O. Naaman, M. Neeley, C. Neill, M. Y. Niu, T. E. O'Brien, A. Opremcak, B. Pató, A. Petukhov, N. C. Rubin, D. Sank, V. Shvarts, D. Strain, M. Szalay, B. Villalonga, T. C. White, Z. Yao, P. Yeh, J. Yoo, A. Zalcman, H. Neven, S. Boixo, A. Megrant, Y. Chen, J. Kelly, V. Smelyanskiy, A. Kitaev, M. Knap, F. Pollmann, and P. Roushan, Realizing topologically ordered states on a quantum processor, *Science* **374**, 1237 (2021).
- [29] R. Acharya, I. Aleiner, R. Allen, T. I. Andersen, M. Ansmann, F. Arute, K. Arya, A. Asfaw, J. Atalaya, R. Babbush, D. Bacon, J. C. Bardin, J. Basso, A. Bengtsson, S. Boixo, G. Bortoli, A. Bourassa, J. Bovaird, L. Brill, M. Broughton, B. B. Buckley, D. A. Buell, T. Burger, B. Burkett, N. Bushnell, Y. Chen, Z. Chen, B. Chiaro, J. Cogan, R. Collins, P. Conner, W. Courtney, A. L. Crook, B. Curtin, D. M. Debroy, A. Del Toro Barba, S. Demura, A. Dunsworth, D. Eppens, C. Erickson, L. Faoro, E. Farhi, R. Fatemi, L. Flores Burgos, E. Forati, A. G. Fowler, B. Foxen, W. Giang, C. Gidney, D. Gilboa, M. Giustina, A. Grajales Dau, J. A. Gross, S. Habegger, M. C. Hamilton, M. P. Harrigan, S. D. Harrington, O. Higgott, J. Hilton, M. Hoffmann, S. Hong, T. Huang, A. Huff, W. J. Huggins, L. B. Ioffe, S. V. Isakov, J. Iveland, E. Jeffrey, Z. Jiang, C. Jones, P. Juhas, D. Kafri, K. Kechedzhi, J. Kelly, T. Khattar, M. Khezri, M. Kieferová, S. Kim, A. Kitaev, P. V. Klimov, A. R. Klotz, A. N. Korotkov, F. Kostritsa, J. M. Kreikebaum, D. Landhuis, P. Laptev, K.-M. Lau, L. Laws, J. Lee, K. Lee, B. J. Lester, A. Lill, W. Liu, A. Locharla, E. Lucero, F. D. Malone, J. Marshall, O. Martin, J. R. McClean, T. McCourt, M. McEwen, A. Megrant, B. Meurer Costa,

- X. Mi, K. C. Miao, M. Mohseni, S. Montazeri, A. Morvan, E. Mount, W. Mruczkiewicz, O. Naaman, M. Neeley, C. Neill, A. Nersisyan, H. Neven, M. Newman, J. H. Ng, A. Nguyen, M. Nguyen, M. Y. Niu, T. E. O'Brien, A. Opremcak, J. Platt, A. Petukhov, R. Potter, L. P. Pryadko, C. Quintana, P. Roushan, N. C. Rubin, N. Saei, D. Sank, K. Sankaragomathi, K. J. Satzinger, H. F. Schurkus, C. Schuster, M. J. Shearn, A. Shorter, V. Shvarts, J. Skrzuzny, V. Smelyanskiy, W. C. Smith, G. Sterling, D. Strain, M. Szalay, A. Torres, G. Vidal, B. Villalonga, C. Vollgraff Heidweiller, T. White, C. Xing, Z. J. Yao, P. Yeh, J. Yoo, G. Young, A. Zalcman, Y. Zhang, N. Zhu, and Google Quantum AI, Suppressing quantum errors by scaling a surface code logical qubit, *Nature* **614**, 676 (2023).
- [30] F. Bao, H. Deng, D. Ding, R. Gao, X. Gao, C. Huang, X. Jiang, H.-S. Ku, Z. Li, X. Ma, X. Ni, J. Qin, Z. Song, H. Sun, C. Tang, T. Wang, F. Wu, T. Xia, W. Yu, F. Zhang, G. Zhang, X. Zhang, J. Zhou, X. Zhu, Y. Shi, J. Chen, H.-H. Zhao, and C. Deng, Fluxonium: An Alternative Qubit Platform for High-Fidelity Operations, *Phys. Rev. Lett.* **129**, 010502 (2022).
- [31] V. E. Manucharyan, J. Koch, L. I. Glazman, and M. H. Devoret, Fluxonium: Single Cooper-Pair Circuit Free of Charge Offsets, *Science* **326**, 113 (2009).
- [32] F. Yan, S. Gustavsson, A. Kamal, J. Birenbaum, A. P. Sears, D. Hover, T. J. Gudmundsen, D. Rosenberg, G. Samach, S. Weber, J. L. Yoder, T. P. Orlando, J. Clarke, A. J. Kerman, and W. D. Oliver, The Flux Qubit Revisited to Enhance Coherence and Reproducibility, *Nature Communications* **7**, 12964 (2016).
- [33] One may generalize the charge operator $\hat{n} \rightarrow \hat{n} - n_g$ to include an offset n_g describing the influence of an external gate voltage or of environmental charge fluctuation. However, for our purposes, these effects are of little relevance.
- [34] J. M. Gambetta, Control of Superconducting Qubits, in *Quantum Information Processing: Lecture Notes of the 44th IFF Spring School 2013*, Schriften Des Forschungszentrums Jülich Reihe Schlüsseltechnologien No. Bd. 52, edited by D. DiVincenzo (2013) pp. B4.1–B4.50.
- [35] S. Rosenblatt, J. Hertzberg, M. Brink, J. Chow, J. Gambetta, Z. Leng, A. Houck, J. J. Nelson, B. Plourde, X. Wu, R. Lake, J. Shainline, D. Pappas, U. Patel, and R. McDermott, Variability metrics in Josephson Junction fabrication for Quantum Computing circuits, in *APS March Meeting Abstracts*, APS Meeting Abstracts, Vol. 2017 (2017) p. Y46.002.
- [36] J. M. Gambetta, J. M. Chow, and M. Steffen, Building logical qubits in a superconducting quantum computing system, *npj Quantum Information* **3**, 1 (2017).
- [37] R. Barends, J. Kelly, A. Megrant, A. Veitia, D. Sank, E. Jeffrey, T. C. White, J. Mutus, A. G. Fowler, B. Campbell, Y. Chen, Z. Chen, B. Chiaro, A. Dunsworth, C. Neill, P. O'Malley, P. Roushan, A. Vainsencher, J. Wenner, A. N. Korotkov, A. N. Cleland, and J. M. Martinis, Superconducting quantum circuits at the surface code threshold for fault tolerance, *Nature* **508**, 500 (2014).
- [38] S. Sheldon, E. Magesan, J. M. Chow, and J. M. Gambetta, Procedure for systematically tuning up cross-talk in the cross-resonance gate, *Phys. Rev. A* **93**, 060302 (2016).
- [39] S.-D. Börner, *Classical Chaos in Transmon Qubit Arrays*, Bachelor Thesis, University of Cologne (2020).
- [40] C. Timm, *Theoretische Mechanik* (2022).
- [41] J. Pöschel, A lecture on the classical KAM theorem, (2009), arXiv:0908.2234.
- [42] R. Ketzmerick, *Chaos and Quantum Chaos* (2021).
- [43] S.-D. Börner, C. Berke, S. Trebst, and A. Altland, in preparation, (2023).
- [44] O. Mansikkamäki, S. Laine, A. Piltonen, and M. Silveri, Beyond Hard-Core Bosons in Transmon Arrays, *PRX Quantum* **3**, 040314.
- [45] To obtain this representation, one passes from number and phase to an oscillator basis, $(\hat{n}, \hat{\varphi}) \rightarrow \sqrt{\hat{n}} \exp(i\hat{\varphi}) \equiv a$. An expansion of the cos-potential near its minimum up to quartic order then yields the Hubbard Hamiltonian $\hat{H}(a, a^\dagger)$.
- [46] D. J. Luitz, F. Alet, and N. Laflorencie, Universal behavior beyond multifractality in quantum many-body systems, *Phys. Rev. Lett.* **112**, 057203 (2014).
- [47] D. Sels and A. Polkovnikov, Dynamical Obstruction to Localization in a Disordered Spin Chain, *Phys. Rev. E* **104**, 054105 (2021).
- [48] P. D. Bönninghaus, *Chaotic Instabilities in the Classical Limit of IBM Transmon Qubit Designs*, Bachelor Thesis, University of Cologne (2021).
- [49] G. Benettin, L. Galgani, and J.-M. Strelcyn, Kolmogorov entropy and numerical experiments, *Phys. Rev. A* **14**, 2338 (1976).
- [50] G. Datsieris, DynamicalSystems.jl: A Julia software library for chaos and nonlinear dynamics, *Journal of Open Source Software* **3**, 598 (2018).
- [51] G. Benettin, L. Galgani, A. Giorgilli, and J.-M. Strelcyn, Lyapunov Characteristic Exponents for smooth dynamical systems and for hamiltonian systems; a method for computing all of them. Part 1: Theory, *Meccanica* **15**, 9 (1980).
- [52] G. Benettin, L. Galgani, A. Giorgilli, and J.-M. Strelcyn, Lyapunov Characteristic Exponents for smooth dynamical systems and for hamiltonian systems; A method for computing all of them. Part 2: Numerical application, *Meccanica* **15**, 21 (1980).
- [53] C. Rackauckas and Q. Nie, DifferentialEquations.jl – A Performant and Feature-Rich Ecosystem for Solving Differential Equations in Julia, *Journal of Open Research Software* **5**, 15 (2017).
- [54] C. Tsitouras, Runge–Kutta pairs of order 5(4) satisfying only the first column simplifying assumption, *Computers & Mathematics with Applications* **62**, 770 (2011).
- [55] J. H. Verner, Explicit Runge-Kutta Methods with Estimates of the Local Truncation Error, *SIAM Journal on Numerical Analysis* **15**, 772 (1978).
- [56] G. S. Paraoanu, Microwave-Induced Coupling of Superconducting Qubits, *Phys. Rev. B* **74**, 140504 (2006).
- [57] E. Magesan and J. M. Gambetta, Effective Hamiltonian Models of the Cross-Resonance Gate, *Phys. Rev. A* **101**, 052308 (2020).
- [58] V. Tripathi, M. Khezri, and A. N. Korotkov, Operation and Intrinsic Error Budget of a Two-Qubit Cross-Resonance Gate, *Phys. Rev. A* **100**, 012301 (2019).
- [59] F. Pietracaprina, N. Macé, D. J. Luitz, and F. Alet, Shift-invert diagonalization of large many-body localizing spin chains, *SciPost Phys.* **5**, 045 (2018).

APPENDIX

We complement our discussion of the main text with three short Appendices. The first one provides a compact introduction to the concept of Lyapunov exponents in classical chaos theory, a concept routinely used in our analysis, and its numerical computation. The second Appendix gives supporting documentation of the level of fluctuations of Josephson energies in current-generation IBM devices. The third Appendix provides technical background information on the algorithmic

scaling of our numerical approach and the required compute times to simulate systems with 4,000+ coupled transmons.

1. Lyapunov exponents

In the main body of this paper, we quantify classical in terms of the maximal Lyapunov exponent λ , i.e. the rate of divergence of initially nearby trajectories. Consider the difference vector $\delta\pi = \pi - \pi'$ of two trajectories $\pi = (\mathbf{q}, \mathbf{p})$ and $\pi' = (\mathbf{q}', \mathbf{p}')$ in the $2S$ dimensional phase space. Linearizing the equations of motion for small $\delta\pi$ yields

$$\delta\dot{\pi} = \mathbf{M}\delta\pi. \quad (9)$$

The matrix \mathbf{M} contains the second derivatives of the Hamilton function with respect to \mathbf{q} and \mathbf{p} . With the ansatz $\delta\pi(t) = \pi_0 \exp(\lambda t)$, one arrives at the eigenvalue equation

$$\mathbf{M}\pi_0 = \lambda\pi_0. \quad (10)$$

The eigenvalues λ are referred to as *Lyapunov exponents*. Phase space area conservation (Liouville theorem) imply that the spectrum of exponents is organized in pairs of opposite sign $\pm\lambda$, where the existence of non-zero eigenvalues is an indication of chaos. The exponent of largest modulus then determines the rate at which generic phase space separations $\delta\pi$ diverge, and therefore is the prime quantifier of chaotic instability. We refer to this maximal exponent as λ throughout.

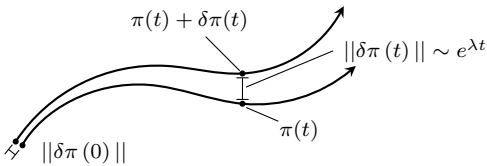


FIG. 18. **Lyapunov exponents** determine the rate at which two trajectories $\pi(t)$ and $\pi(t) + \delta\pi(t)$ diverge as $\|\delta\pi(t)\| \sim \exp(\lambda t)$.

In the main text, we compute the exponents by a method proposed by Benettin [49], where two nearby trajectories are evolved in time and the distance vector is repeatedly rescaled at preserved direction. The time after the divergence exceeds a certain phase space distance threshold $\|\delta\pi\|$ then determines λ , for details see the original paper [49] or Ref. [50]. To cross-check the results, we also compute the complete Lyapunov spectrum via an alternative method, known as ‘H2’ [51, 52]. In either case, we use the implementation provided by the software library DynamicalSystems.jl [50] that in turn is based on DifferentialEquations.jl [53]. The equations of motion are solved using the implementation of Tsitouras 5/4 Runge-Kutta method [54]. It was checked that the results for λ are unchanged if higher-order methods (Verner’s ‘‘Most Efficient’’ 7/6 Runge-Kutta method [55]), lower error thresholds and longer evolution times (the exact λ is obtained as a $t \rightarrow \infty$ limit) are used.

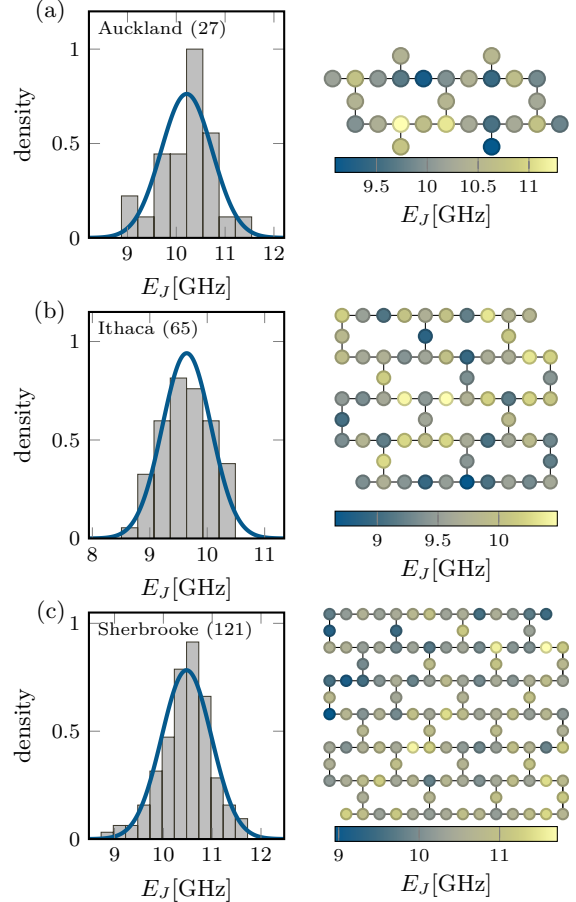


FIG. 19. **Examples of IBM’s fixed frequency architectures.** Shown is the distribution of Josephson energies for one instance of each processor generation, Falcon (27 qubits), Hummingbird (65 qubits) and Eagle (121 qubits), available in the IBM Quantum Cloud [18]. The E_J spreading is consistent with Gaussian disorder (despite some post-fabrication fine-tuning).

2. Disordered transmon arrays

A widely used, hardware-efficient entangling gate in fixed-frequency architectures is the cross-resonance (CR) gate [26, 56], that switches on a ZX interaction by driving one qubit with a neighboring qubit’s frequency. Effective models for the CR gate [57, 58] show that a small ratio of anharmonicity and qubit frequency detuning $\delta\nu_q = \nu_1 - \nu_2$, i.e., $\frac{E_C}{\hbar\delta\nu_q} < 1$, weakens the strength of the effective interaction and thereby slows down the gate. In state-of-the-art fixed frequency processors, one typically finds a detuning of $\hbar\delta\nu_q \approx \frac{E_C}{2}$, which we take to be the definition of the disorder strength. In the transmon regime $E_J \gg E_C$, the qubit frequencies are well approximated by $\hbar\nu_q \approx \sqrt{8E_C E_J} - E_C$ [4], such that a scaling of the Josephson energy spread δE_J according to $\delta E_J = \sqrt{E_J E_C}/8$, as exploited in Sec. III B, guarantees the desired frequency detuning. In addition, in the experimentally core region of $E_J \lesssim 40$ GHz, the above choice of $\delta\nu_q$ reproduces a variation of several hundred MHz in the Josephson

energies, in broad agreement with typical values of the as-fabricated ‘natural’ disorder in fixed-frequency architectures, see Fig. 19. For the data shown in Fig. 9, we consider larger disorders while maintaining the typical square root scaling of δE_J with the average Josephson energy.

3. Algorithmic scaling

A difficulty in the exact diagonalization of the quantum mechanical system is the transmon’s bosonic nature leading to faster growth of the Hilbert space dimension n than the computational space of a qubit system. Even when exploiting the approximate conservation of particle number [7], and considering the different blocks of the Hamiltonian in (3) with a fixed total excitation number N separately, the resulting matrices have dimensions $(N + L - 1)! / ((L - 1)! N!)$, where L is the number of transmons. At half-filling (the situation most commonly studied in this work and previous studies [6, 7]), this yields an approximate scaling of $n \approx 2.6^L / \sqrt{L}$ for large L [6] – an exponentially faster growth than the corresponding sector with equal numbers of 0’s and 1’s in the computational subspace whose dimension scales as $2^L / \sqrt{L}$ [59]. This naturally implies that exact diagonalization studies of coupled transmon arrays are restricted to small systems, i.e., $L \lesssim 18$ even when using shift-invert diagonalization techniques to extract *individual* eigenvectors at high energies [6, 59]. For the results in Fig. 9 we average, for each disorder realization, the IPR over *many* eigenstates obtained by full diagonalization of the $N = 5$ block of a 10-transmon chain.

For the classical simulation, using an explicit ODE solver [53] for the calculation of the Lyapunov exponents, the effort for a single time-step propagation grows linear in system

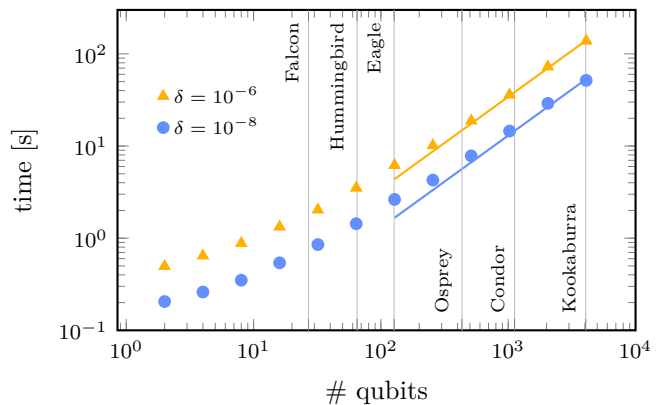


FIG. 20. **Compute times for the classical simulations.** Shown are measurements of the compute time per core (of an Intel(R) Core(TM) i5-8400 CPU @ 2.80GHz) of the classical simulation of different length transmon chains, for initial state $|101010\dots\rangle$, $E_C = 250$ MHz, $E_J = 10$ GHz, $\delta E_J = 559$ MHz and $T = 50$ Mhz, with different absolute and relative error tolerances δ . The given lines are linear fits for the longest five time values of each data set, showing the asymptotic behaviour. All calculated Lyapunov exponents have 10,000 underlying time steps.

size. Naturally, the number of steps of the differential equation solver also enters in the computational complexity. We find that the number of steps needed for a desired accuracy during the integration of the equations of motion does not increase with the size of the transmon array and is a roughly constant value, such that the overall computational complexity to determine the Lyapunov exponent should grow linearly in the number of transmons L . This is in good agreement with the asymptotic behavior for large system sizes shown in Fig. 20. Note that the numerically obtained value of λ approaches the exact result only in the limit $t \rightarrow \infty$ where t is the total evolution time. The computational time increases linearly with the total evolution time t . Comparing the results for λ obtained with different t ranging from 10^3 to $5 \cdot 10^5$, we find that convergent results are typically obtained $t \approx \mathcal{O}(10^4)$ time steps, such that, for example, analyzing one of IBM’s ‘Hummingbird’ processors containing 65 qubits takes ≈ 3.5 s for an error tolerance (both relative and absolute) of 10^{-8} in the integration of the differential equations.